The Astrophysical Journal, 915:30 (11pp), 2021 July 1 https://doi.org/10.3847/1538-4357/ac004e

Numerical Research on the Effect of the Initial Parameters of a CME Flux-rope Model on Simulation Results. II. Different Locations of Observers

Fang Shen[1,2,3], Yousheng Liu[1,2], and Yi Yang[1,2]

[1] SIGMA Weather Group, State Key Laboratory of Space Weather, National Space Science Center, Chinese Academy of Sciences, Beijing, 100190, People's Republic of China; fshen@spaceweather.ac.cn

[2] College of Earth and Planetary Sciences, University of Chinese Academy of Sciences, Beijing, 100049, People's Republic of China

Received 2021 March 25; revised 2021 April 28; accepted 2021 May 10; published 2021 July 1

Abstract

In numerical studies of the initiation and propagation of coronal mass ejections (CMEs), it has been proven that the shape, size, and plasma parameters of CMEs could significantly affect simulation results and subsequent space weather predictions. In our previous research, we proposed a new way to initiate a CME based on the graduated cylindrical shell model, and studied the effect of different initial parameters of CMEs on the simulation results when the observer is aligned with the initial propagation direction of the CME. In this paper, we investigate the influence of the different initial parameters of CMEs on simulation results at the observational points with different longitudes and latitudes. Our results indicate that as long as the initial mass of the CME remains unchanged, the initial geometric thickness will have a different influence in the latitudinal and longitudinal directions. The deflection of the CMEs always occurs in both latitudinal and longitudinal directions, when the CMEs interact with the background solar wind structures, such as the corotating interaction region, in the heliosphere.

Unified Astronomy Thesaurus concepts: Magnetohydrodynamical simulations (1966); Solar coronal mass ejections (310); Solar wind (1534); Space weather (2037)

1. Introduction

It is well-known that coronal mass ejections (CMEs) play an important role in space weather. Studies about the origin, the structure, and the propagation of CMEs are essential to space weather research.

Magnetohydrodynamic (MHD) simulation is an important tool for studying the evolution of a CME in both corona and the interplanetary space, and the modeled results can be used to analyze the initiation and propagation characteristics observed by ground-based and space-based instruments (e.g., Chen 2011; Webb & Howard 2012; Cheng et al. 2017; Toriumi & Wang 2019). When modeling the CMEs erupting from the solar source regions and their propagating characteristics, the initial parameters of CMEs, such as their density, velocity, magnetic field, and geometry, can affect the simulation results at the observers in the interplanetary space (Chané et al. 2006; Scolini et al. 2018; Hosteaux et al. 2019; Shen et al. 2021). The cone model, the flux-rope model, the spherical plasmoid model, and the magnetized plasma blob model are popular models to specify the initialization of CMEs in recent years (e.g., Odstrcil & Pizzo 1999; Vandas et al. 2002; Chané et al. 2005; Thernisien et al. 2006; Shen et al. 2007, 2011c, 2013, 2014; Thernisien 2011; Manchester & van der Holst 2014; Shiota & Kataoka 2015; Zhou & Feng 2016). The effect of the different parameters in the CME initialization models on simulation results also have been analyzed by many authors. Scolini et al. (2018) used the cone model as the CME initialization model to study the effect of different CME shapes on the simulation results, and showed that all the parameters specifying the shape of the CME significantly affected the simulation results at 1 au. Chané et al. (2005) used the blob CME model to study how the initial magnetic polarity influenced the evolution of the CME shocks. Using the magnetized plasma blob CME initialization model, Hosteaux et al. (2019) investigated the influence of the different initial velocities of both normal and inverse CMEs on the evolution of the CMEs up to 1 au.

In our previous study (Shen et al. 2021, cited as Paper I hereafter), we established a CME flux-rope model based on the graduated cylindrical shell (GCS) model, and studied the effect of the initial CME parameters on the simulation results at the observers located in the directions aligned with the initial propagating direction of the CME. The simulation results showed that when the initial density and geometric size of the CME changed at the same time, both of them affected the propagation of the CME; when the initial density and geometric size of the CME changed but the total mass remained approximately the same, the propagation of the CME was not affected much. We also found that when the initial magnetic field strength increased, both the peak value of the total magnetic field and the duration time of the prominence of B_{total} and B_z increased obviously. Furthermore, when the magnetic field reversed its direction, the B_z also reversed its direction; but other parameters, such as the density, velocity, and total B, almost remain unchanged both at the Earth and Mars.

In this paper, we extend the previous work to study the influence of the different CME initial parameters on the simulation results at locations with different longitudes and latitudes. The organization of the paper is as follows. We describe the numerical models in Section 2. In Section 3, we compare the simulation results of CMEs with different initial parameters. In Section 4, we conclude.

---

[3] Corresponding author: SIGMA Weather Group, State Key Laboratory of Space Weather, National Space Science Center, Chinese Academy of Sciences, Beijing, 100190, China.

2. Three-dimensional MHD Model and Simulation Method

In this section, we present the 3D MHD simulation of the background for Carrington rotation (CR) 2093. The computational domain here covers $21.5R_s \leqslant r \leqslant 453R_s$, $-90° \leqslant \theta \leqslant 90°$, and $0° \leqslant \phi \leqslant 360°$, where r is the radial distance from solar center in units of solar radius R_s, and θ and ϕ are the elevation and azimuthal angles, in units of degrees, respectively. The grid mesh is built to be $308(r) \times 180(\theta) \times 360(\phi)$. The grid size is uniform in the longitudinal and latitudinal directions with $\Delta\theta = 1°$ and $\Delta\phi = 1°$; in the radial direction, the grid size gradually changes from about $0.37R_s$ at the inner boundary of $21.5R_s$ to $3.61R_s$ at the outer boundary near $453R_s$.

The numerical scheme we used to construct the background solar wind is a 3D interplanetary total variation diminishing (IN-TVD) scheme (e.g., Shen et al. 2018, 2021; Liu et al. 2019) in a Sun-centered spherical coordinate system (r, θ, ϕ). During the simulation, we use a six-component mesh grid system on the spherical shell to avoid the singularity in the spherical coordinate system (e.g., Feng et al. 2010; Shen et al. 2018). This grid system consists of six identical component meshes to envelope a spherical surface with partial overlap on their boundaries. Each component grid is a low-latitude spherical mesh, which is defined in the spherical coordinates by Feng et al. (2010), where δ is proportionally dependent on the grid spacing entailed for the minimum overlapping area.

The inner boundary ($21.5R_s$) is located beyond the Alfvén critical surface, which means that a given boundary condition will determine the evolution of the solar wind in interplanetary space. According to the Wang–Sheeley–Arge empirical model (Arge et al. 2003), we initialize the distribution of the solar wind velocity at the inner boundary with the distribution of f_s and θ_b on the source surface. Here f_s is the expansion factor of magnetic field, defined as $B_s R_s^2 / B_{ss} R_{ss}^2$, where B_s and B_{ss} are the magnetic field strength on the photosphere and on the source surface, respectively; R_s and R_{ss} are the radius of the Sun and of the source surface, respectively. θ_b is the minimum angular distance from the footpoint of the magnetic field line at the Sun's surface to the nearest coronal hole boundary. Both f_s and θ_b can be obtained based on the potential field source surface (PFSS) model (Altschuler & Newkirk 1969; Schatten et al. 1969) of the coronal magnetic field and the magnetogram provided by the Global Oscillation Network Group project. The distribution of the magnetic field at the inner boundary is also given based on the PFSS model.

After established the steady-state background solar wind (see, e.g., Shen et al. 2018; Liu et al. 2019), we input the CME model to the ambient solar wind. The CME is initialized based on the GCS model, as described in our previous studies (e.g., Liu et al. 2019; Shen et al. 2021). This kind of CME initialization model consists of two main parts: two conical legs and a curved front, which is reminiscent of a torus with its cross section increasing with height.

Figure 1 shows a set of CME initialization models with different geometric thickness. In this CME model, the geometric thickness is described by the half-angle of the cone, which is noted as δ in Figure 1. The geometric relationship of the varying radius could be given by $a(r) = r\sin(\delta)$, where r is the distance from a point on the shell to the center of the Sun. The angle between the axis of two conical legs is 2α and the height of the cone is h, as shown in Figure 1. The detailed description of the geometric parameters can be found in Liu et al. (2019).

The magnetic field distribution of the CME model is given based on the Lundquist flux-rope model in cylindrical coordinate, shown as below:

$$\begin{cases} B_r = 0 \\ B_\phi = \sigma_h B_{\max} J_1(\alpha r), \\ B_z = \sigma_h B_{\max} J_0(\alpha r) \end{cases} \tag{1}$$

where J_1 and J_0 are the first-order and zero-order Bessel function, respectively; $\sigma_h = \pm 1$ is the helicity sign, which stands for the direction of magnetic field; α is the force-free parameter; and $B_{\max}$ is the maximum of the magnetic field, which can be written as:

$$B_{\max} = \sqrt{\frac{2.405 H_m}{4\pi LRJ}}, \tag{2}$$

where

$$J = \int_0^R J_1^2(\alpha r) dr, \tag{3}$$

H_m is the magnetic helicity of the Lundquist flux rope (Lundquist 1951), and L is the flux-rope length, which can be written as:

$$L = 2\omega(H_{\rm front} - R_{\rm front}), \tag{4}$$

where ω is the half-angular width of the GCS model, $H_{\rm front}$ and $R_{\rm front}$ are the maximum height and maximum radius of the front.

At the edge of the CME flux rope, the axial component of the magnetic field is assumed to be zero. Therefore, when $r = R$, J_0'll has its first zero value, where R stands for the radius of the cylindrical shell, and we can easily get (e.g., Dasso et al. 2006) $\alpha R = 2.405$.

The density, radial velocity, and temperature profile of the initial perturbation are defined as follows:

$$\begin{cases} \rho_{\rm cme} = \rho_{\max}\left(1 - \frac{D^2}{(2R)^2}\right) \\ V_{\rm cme} = V_{\max}\left(1 - \frac{D^2}{(2R)^2}\right) \\ T_{\rm cme} = T_{\max}\left(1 - \frac{D^2}{(2R)^2}\right). \end{cases} \tag{5}$$

The total density, radial velocity, and temperature of the CME area can be written as:

$$\begin{cases} \rho_{\rm total} = \rho_{\rm cme} + \rho_0 \cdot \frac{D^2}{(2R)^2} \\ V_{\rm total} = V_{\rm cme} + V_0 \cdot \frac{D^2}{(2R)^2} \\ T_{\rm total} = T_{\rm cme} + T_0 \cdot \frac{D^2}{(2R)^2}. \end{cases} \tag{6}$$

At the front part, R is the radius of the cross section at the point, and D stands for the distance to the center point B. At the part of conical legs, R still represents the radius of the cross section, but D is defined as the distance to the inner side of the cone in

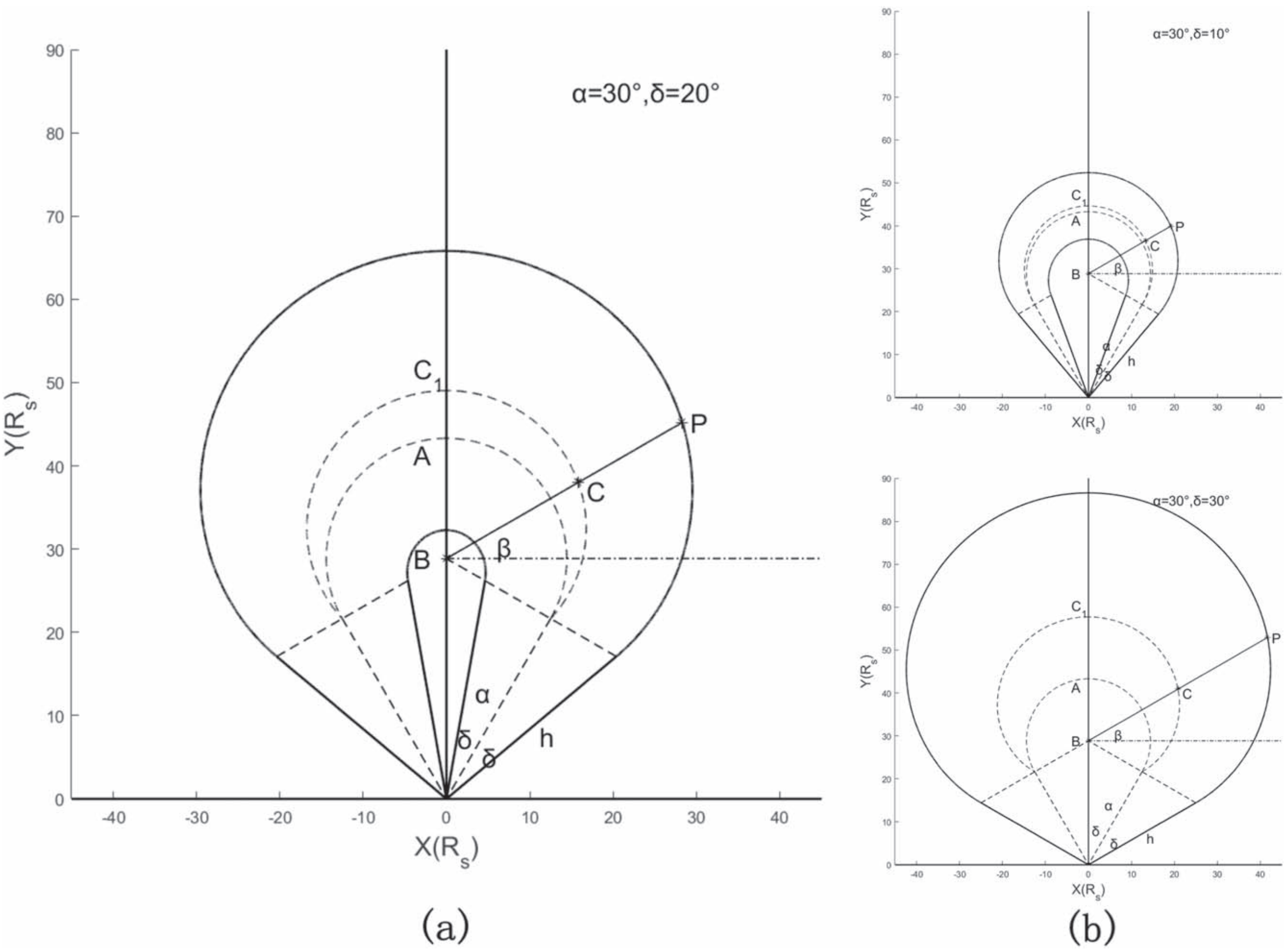

Figure 1. Schematic of the GCS models with different geometric thicknesses. (a) $\alpha = 30°$ and $\delta = 20°$ (standard case); (b) $\alpha = 30°$ and $\delta = 10°$ and 30°.

the cross section plane. $\rho_{\max}$, $V_{\max}$, and $T_{\max}$ are the maximum density, radial velocity, and temperature of the CME. ρ_0, V_0, and T_0 are the density, radial velocity, and temperature of the background solar wind, respectively.

3. CME Case Selection and Simulation Results at Different Locations

3.1. CME Case Selection and Observers' Locations

To study the influence of the initial CME parameters on the simulation results at different locations, we choose five cases with different initial parameters, including density, geometric thickness, and magnetic field, as shown in Table 1. In Paper I, we demonstrated that when the initial density and geometric dimension of CME changed simultaneously, both of them could affect the propagation of the CME and the simulation results at Earth and Mars, while if keeping the total mass of CME almost unchanged and varying the initial density and geometric dimension of CME, the simulation results along the initial CME propagating direction do not change significantly. If we move the observers away from the direction of the initial CME's direction, how will the simulation results change?

In this research, we keep the total mass of the CME unchanged, and set three CME cases to study the effect of the different geometric dimension with δ set to 10°, 20° (standard case), and 30°. As seen in Figure 1, δ determines the thickness of the CME flux tube. In order to keep the total mass of the CME in the three cases almost the same, the densities of the initial CMEs are set to 1, 5.42, and 0.267, in units of $10^{-18}\,\mathrm{kg\,m^{-3}}$, corresponding to δ of 20° (standard case), 10°, and 30°, as in Cases 1 to 3 shown in Table 1. The calculation process of the total CME mass can be found in Paper I, and we do not provide it here. We also have another two cases with different initial magnetic fields, as in Cases 4 and 5 shown in Table 1. In Cases 4 and 5, the values of the initial magnetic field helicity, $B_{\max}$, are set to be 500% and 20% of the value in Case 1, respectively.

3.2. Simulation Results

It takes about 400 hr to reach the MHD equilibrium state for the background solar wind. Figure 2 shows the distribution of radial velocity of background solar wind at the meridional plane and the ecliptic plane, where the different longitudinal and latitudinal locations of observers are plotted by red dots.

After the ambient solar wind is established, the initial CME is launched based on the GCS model toward the Earth. The CME parameters of the five cases are shown in the top five rows in Table 1. Figure 3 plots the density N^*, which is defined as follows, at 30 hr after the launch of the CME.

$$N^* = N \cdot \left(\frac{r}{215R_s}\right)^2, \tag{7}$$

Table 1

CME Initial Parameters of the Five Cases and Simulation Results at Seven Locations with Different Latitudes

Common Par.	Direction N0W0									V_{max} 1200 km s^1									T_{max} 1.5×10^6 K									h $25R_s$				α 30°			
Result	Case1							Case2							Case3							Case4							Case5						
δ(deg)	20							10							30							20							20						
ρ_{max} (10^{-18} kg m^{-3})	1.0							5.42							0.267							1.0							1.0						
H_m(10^{42} Mx^2)	1.0							1.0							1.0							5.0							0.2						
Location	S30°	S20°	S10°	Earth	N10°	N20°	N30°	S30°	S20°	S10°	Earth	N10°	N20°	N30°	S30°	S20°	S10°	Earth	N10°	N20°	N30°	S30°	S20°	S10°	Earth	N10°	N20°	N30°	S30°	S20°	S10°	Earth	N10°	N20°	N30°
SAT(hr)	41	32	29	29	29	31	38	43	33	29	29	30	33	41	37	29	27	27	27	28	32	35	30	27	27	27	29	32	43	33	29	29	29	33	38
Peak value of V_r(km s^{-1})	540	850	920	920	930	860	760	530	800	920	940	910	800	750	600	900	920	900	950	920	810	780	940	940	940	1000	920	860	530	780	940	920	920	800	⋯
Peak value of ρ(cm^{-3})	16	17	22	24	18	15	5	11	23	22	23	18	12	5	27	30	23	24	15	20	8	43	28	23	26	17	17	11	12	16	24	24	20	13	4
Peak value of B_{total}(nT)	⋯	6	18	22	16	5	1	⋯	3	12	19	11	1	⋯	2	15	24	26	23	11	1	11	14	24	26	23	15	5	⋯	⋯	12	14	10	⋯	⋯
Peak value of south B_z(nT)	⋯	−1	−7	−10	−5	−1	−1	⋯	−0.5	−4	−9	−3	−2	⋯	⋯	−3	−11	−12	−7	−3	−1	−1	−8	−20	−20	−14	−5	−1	⋯	⋯	−2	−2	−1	⋯	⋯

Note. The top row lists the common initial parameters and the second to fifth rows list the different initial parameters. The common initial parameters (from left to right) are the propagation direction, the maximum velocity and temperature of the initial CME, and the height and the radius of the GCS cone, respectively. Different initial parameters, from the third to fifth rows, are the half-angle of the GCS cone, the maximum number density of the initial CME, and the magnetic helicity of the initial flux rope. From the seventh to eleventh rows: shock arrival time (SAT), peak values of radial velocity (V_r), number density (ρ), total magnetic field (B_{total}), and magnetic field in the z-direction (B_z) for the five cases at seven locations with different latitudes. Note that some results at high latitudes are too small, and we use "⋯" to indicate this.

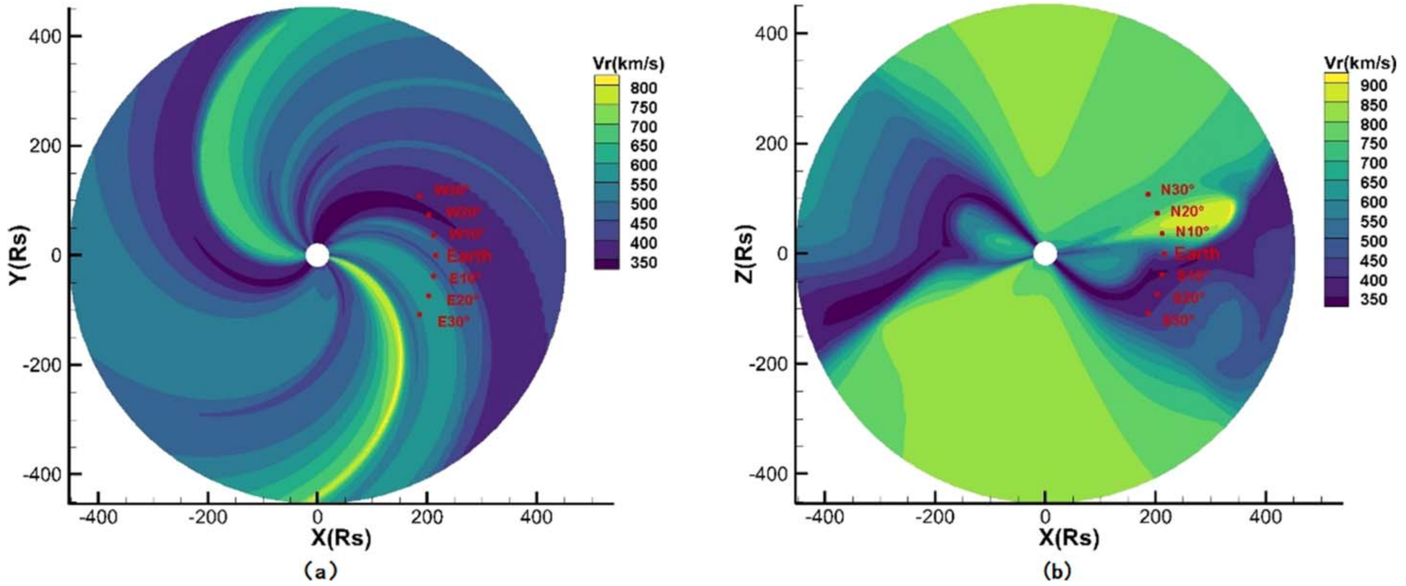

Figure 2. The steady-state distribution of radial velocity at (a) the ecliptic plane and (b) the meridian plane of $\phi = 0°$. The locations of the Earth, longitudes of ±30°, ±20°, and ±10° in panel (a), and latitudes of ±30°, ±20°, and ±10° in panel (b) are marked with red dots.

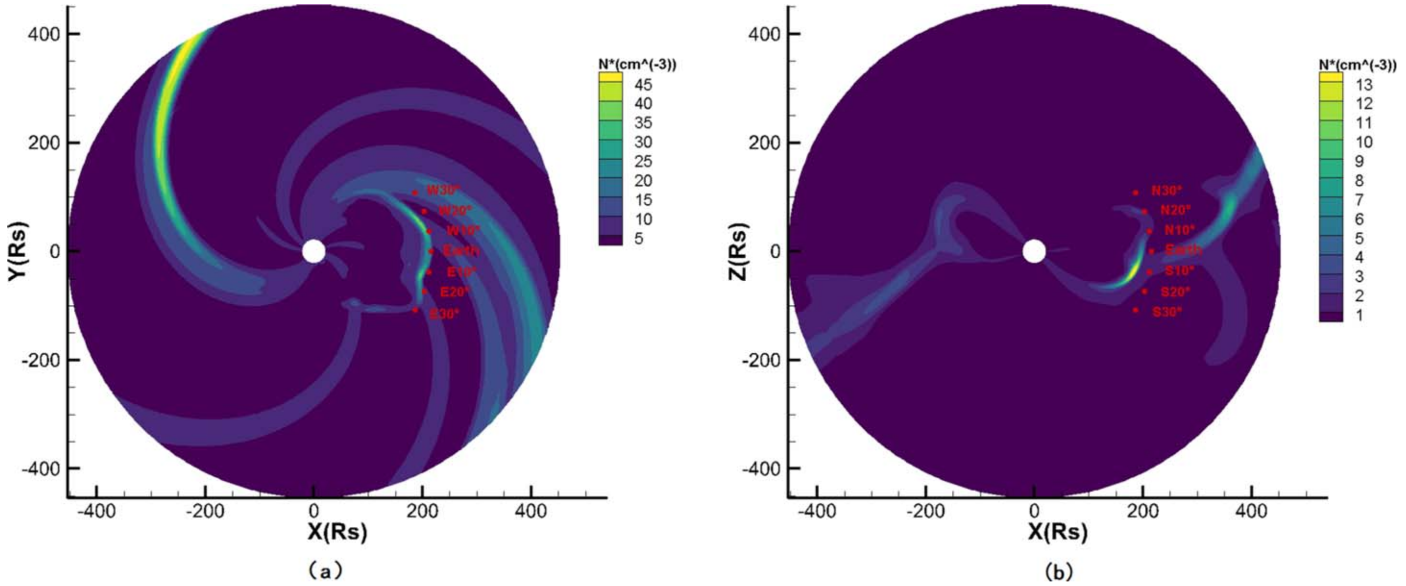

Figure 3. The distribution of density at (a) the ecliptic plane (left panel) and (b) the meridian plane of $\phi = 0°$ at the time of 30 hr after CME launch. The locations of the Earth, longitudes = ±30°, ±20°, and ±10° in panel (a), and latitudes = ±30°, ±20°, and ±10° in panel (b) are marked with red dots.

where r is the radial distance. In this way, the attenuation of density due to the increase in radial distance can be reduced and the difference in the longitudinal direction is shown more clearly (Liu et al. 2019; Shen et al. 2021).

3.2.1. Comparison among Five Cases at 1 au in the Meridian Plane of $\phi = 0°$ with Different Latitudes

In order to study the influence of the initial CME parameters on the properties of the CME at different latitudinal locations in the interplanetary space, we make a series of comparisons among the five cases at seven different latitudinal locations at 1 au, shown as red dots in the panel (b) of Figures 2 and 3. Table 1 summarizes the quantitative comparison among the simulation results of the five cases at the seven latitudinal locations, including the shock arrival time (SAT), peak values of radial velocity, number density, total magnetic field, and south B_z.

Figure 4 shows the distribution of plasma parameters, including density, radial velocity, total magnetic field strength, and B_z, of Cases 1–3 with the same CME initial mass, but with different geometric dimensions. The SATs of Cases 1–3 are shown by the vertical dashed lines in Figure 4.

From panel (a) of Figure 4, the comparison results demonstrate that the profiles at the Earth remain almost the same for the three cases with the same initial CME mass. However, from the other panels of Figure 4 and Table 1, we find that the SATs and the peak values of the parameters are different among the three cases at latitudes of ±10°, ±20°, and ±30°. At the locations away from the CME's initiated propagation direction, as the initial δ increases, which also means the density decreases, the SATs become smaller, and

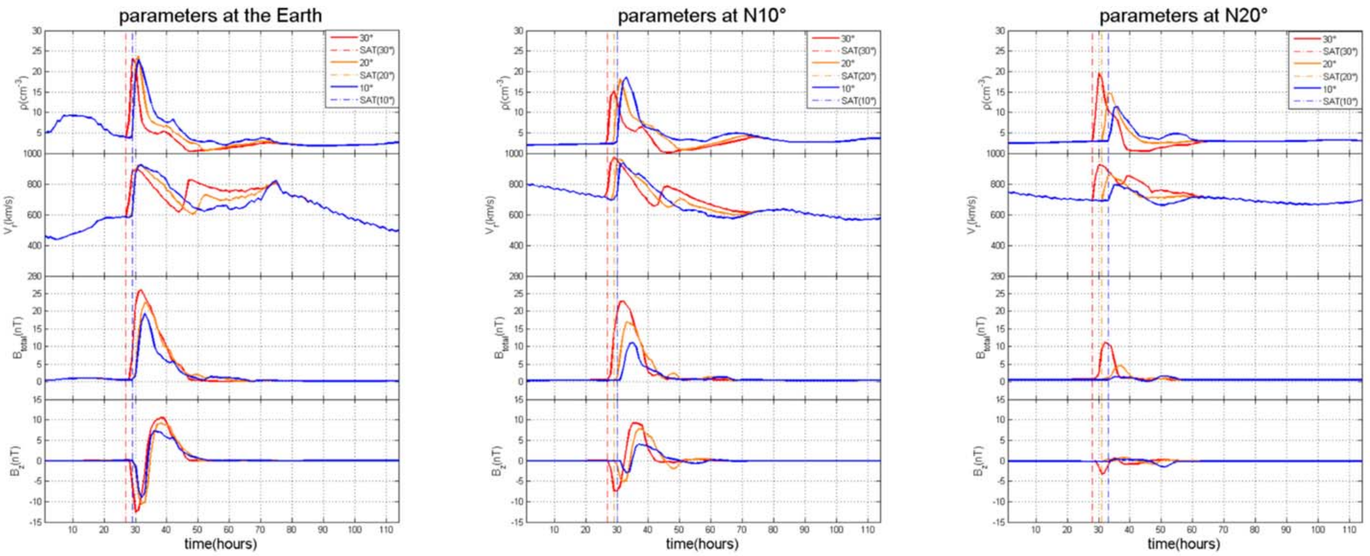

(a) Earth (b) $N10°$ (c) $N20°$

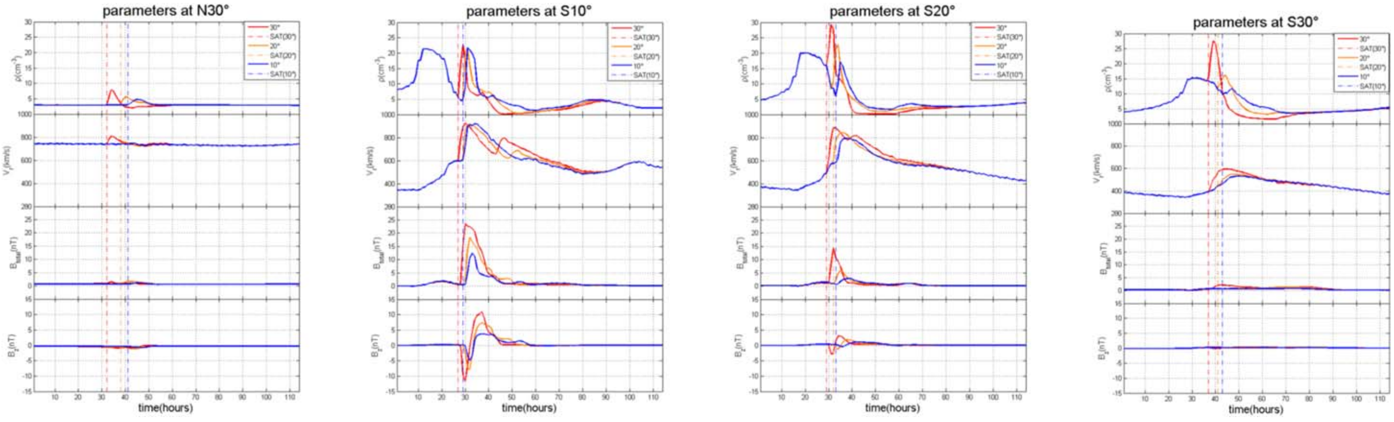

(d) $N30°$ (e) $S10°$ (f) $S20°$ (g) $S30°$

Figure 4. The profiles of plasma parameters—density, radial velocity, total magnetic field strength B_{total}, and B_z—at the Earth (a) and other locations with different latitudes (b)–(g) vs. time after CME launch. Solid lines with different colors refer to Cases 1–3 listed in Table 1 with different initial geometric dimensions: orange, blue, and red lines indicate Cases 1, 2, and 3, respectively. The shock arrival times of different CMEs are marked by dashed–dotted vertical lines with different corresponding colors.

most of the peak values of density, radial velocity, B_{total}, and south of B_z of the CME increase. Moreover, as the latitude increases, the difference of SATs among the three cases becomes larger.

Figure 5 shows the distribution of plasma parameters of Cases 1, 4, and 5 with different initial magnetic field strength. From panels (a), (b), and (d) of Figure 5, we find that at the locations of the Earth, $N10$ and $S10$, the change of the initial magnetic field has little effect on the profiles of the density and velocity curve, but the peak value of the total magnetic field and the duration time of the prominence of B_{total} and B_z are more affected. From panels (c), (d), (f), and (g) of Figure 5, as the initial $B_{\max}$ increases, the SATs get shorter, and most of the peak values of density, radial velocity, B_{total}, and south of B_z of the CME increase. From panels (d) and (g) of Figures 4 and 5, we find that at higher latitudes (>30°), the influence of the CME on the magnetic field is smaller than that on the fluid field. We also find that according to Figures 4 and 5, the distributions of the curves show distinct north–south asymmetry, i.e., the density and the magnetic field strength to the south are larger than that at the same latitudes to the north. The deflection of the CME to the south may be due to the interaction with the corotating interaction region (CIR) structure ahead of the CME, which can be seen in Figure 3(b). Also from Figure 2(b), it can be found that in the background solar wind, there is a CIR region that contains the compressive interaction region with a high-density and low-speed solar wind stream on the south side of the Sun–Earth line. As the fast CME interacts with the compressive interaction region, it will be blocked by the high-density and low-speed solar wind stream, which causes the density and the magnetic field strength to increase, the CME speed to decrease, and the

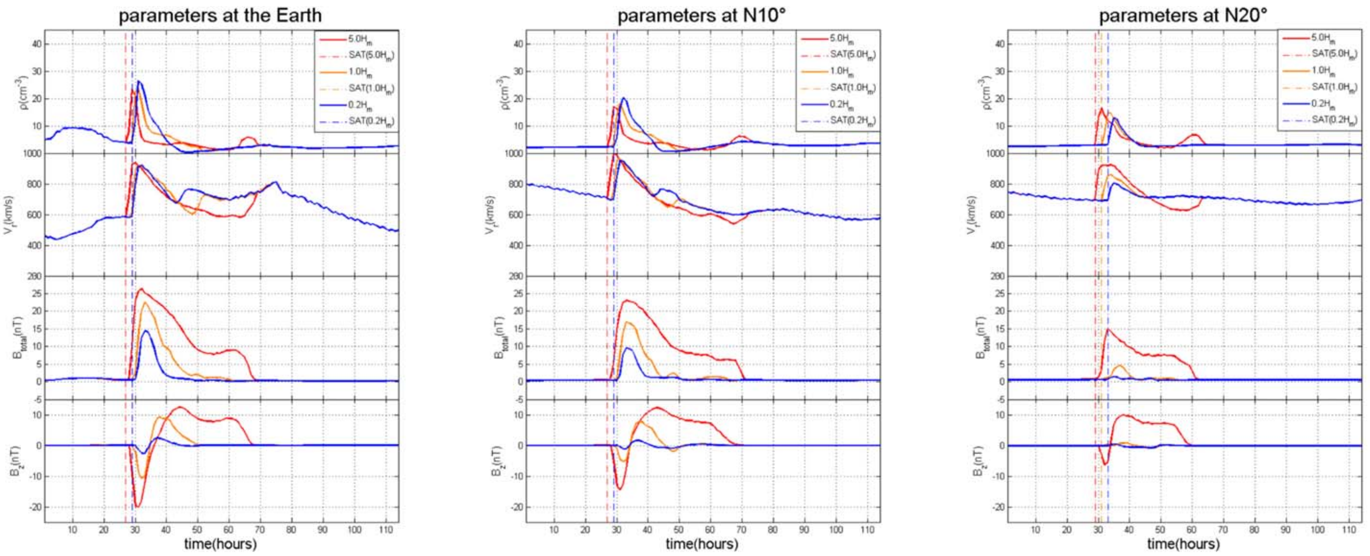

(a) Earth

(b) $N10°$

(c) $N20°$

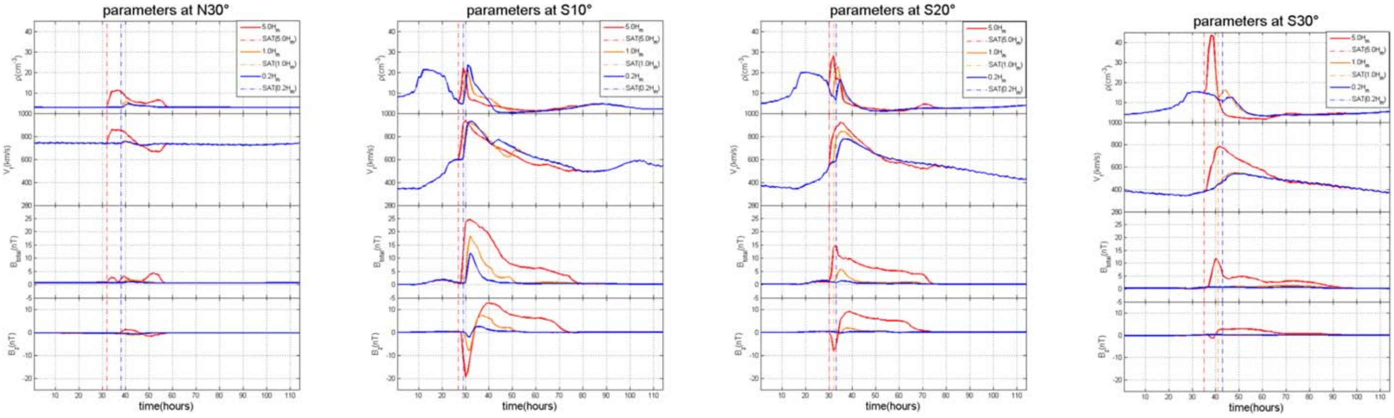

(d) $N30°$

(e) $S10°$

(f) $S20°$

(g) $S30°$

Figure 5. The profiles of plasma parameters—density, radial velocity, total magnetic field strength B_{total}, and B_z—at the Earth (a) and other locations with different latitudes (b)–(g) vs. time after CME launch. Solid lines with different colors refer to Cases 1, 4, and 5 listed in Table 1 with different initial magnetic field strength: orange, red, and blue lines indicate Cases 1, 4, and 5, respectively. The shock arrival times of different CMEs are marked by dashed–dotted vertical lines with different corresponding colors.

shock arrival to delay. And the effect of the CIR can also be found in the prominences before the CME arrival, as shown in panels (e) to (g) in Figures 4 and 5.

3.2.2. Comparison among Five Cases at 1 au in the Ecliptic Plane with Different Longitudes

In this subsection, we make a series of comparisons among the five cases in the ecliptic plane at seven different longitudinal locations at 1 au, shown as red dots in panel (a) of Figures 2 and 3. Table 2 summarizes the quantitative comparison among the simulation results of the five cases at seven different longitudinal locations, including the SATs, peak values of radial velocity, number density, total magnetic field, and south B_z. Figure 6 shows the comparison of the plasma parameters of Cases 1–3 with the same CME initial mass, but with different geometric dimensions at different longitudinal locations (panels (a) to (g)). The SATs of Cases 1–3 are indicated by the vertical dashed lines in Figure 6.

From Table 2 and Figure 6, it can be seen that the SATs at the seven different longitudinal locations are almost the same for the three cases with the same CME initial mass but different geometric dimensions. We find that as the longitudes become larger, all the peak values at the CME shock decrease. Moreover, comparing the curves in each panel of Figure 6, the difference among Cases 1–3 is small at all the locations with different longitudes.

Figure 7 shows the distribution of plasma parameters of Cases 1, 4, and 5 with different initial magnetic field strengths. Based on Table 2 and all the seven panels of Figure 7, the SATs are also almost the same for the three cases. Besides, as the initial $B_{\max}$ increases, most of the values of density and radial velocity change slightly, but B_{total} and south B_z of the CME increase significantly at different longitudinal locations.

Table 2

Simulation Results of the Five Cases at Seven Locations with Different Longitudes From Top to Bottom: Shock Arrival Time (SAT), Peak Values of Radial Velocity (V_r), Number Density (ρ), Total Magnetic Field (B_{total}) and Magnetic Field in the z-direction (B_z), for the Five Cases at Seven Locations with Different Longitudes

Common Par.					Direction N0W0									$V_{\max}$ 1200 km s^{-1}									$T_{\max}$ 1.5 × 10^6 K							h 25R_s			α 30°		
Result				Case1							Case2							Case3							Case4							Case5			
δ(deg)				20							10							30							20							20			
$\rho_{\max}$ (10^{-18} kg m^{-3})				1.0							5.42							0.267							1.0							1.0			
H_m(10^{42}Mx^2)				1.0							1.0							1.0							5.0							0.2			
Location	E30°	E20°	E10°	Earth	W10°	W20°	W30°	E30°	E20°	E10°	Earth	W10°	W20°	W30°	E30°	E20°	E10°	Earth	W10°	W20°	W30°	E30°	E20°	E10°	Earth	W10°	W20°	W30°	E30°	E20°	E10°	Earth	W10°	W20°	W30°
SAT(hr)	36	32	29	29	30	29	29	35	32	29	29	30	29	29	33	31	28	27	28	28	27	35	32	29	27	29	29	28	36	32	29	29	31	29	30
Peak value of V_r(km s^{-1})	640	720	860	920	860	860	920	720	800	940	940	880	940	960	660	680	820	900	860	800	940	640	660	840	940	880	800	900	680	780	940	920	840	940	940
Peak value of ρ(cm^{-3})	20	31	35	24	30	22	7	23	38	36	23	34	27	8	19	30	35	24	30	21	8	18	26	33	26	28	19	7	21	36	38	24	34	30	9
Peak value of B_{total}(nT)	7	21	30	22	25	25	9	10	28	30	19	25	30	10	9	19	30	26	26	24	11	12	18	30	26	28	22	8	6	20	24	14	18	30	8
Peak value of south B_z(nT)	−5	−10	−15	−10	−11	−12	−4	−9	−10	−12	−9	−10	−12	−6	−5	−7	−16	−12	−12	−12	−4	−8	−14	−30	−20	−20	−15	−5	−3	−4	−4	−2	−3	−5	−2

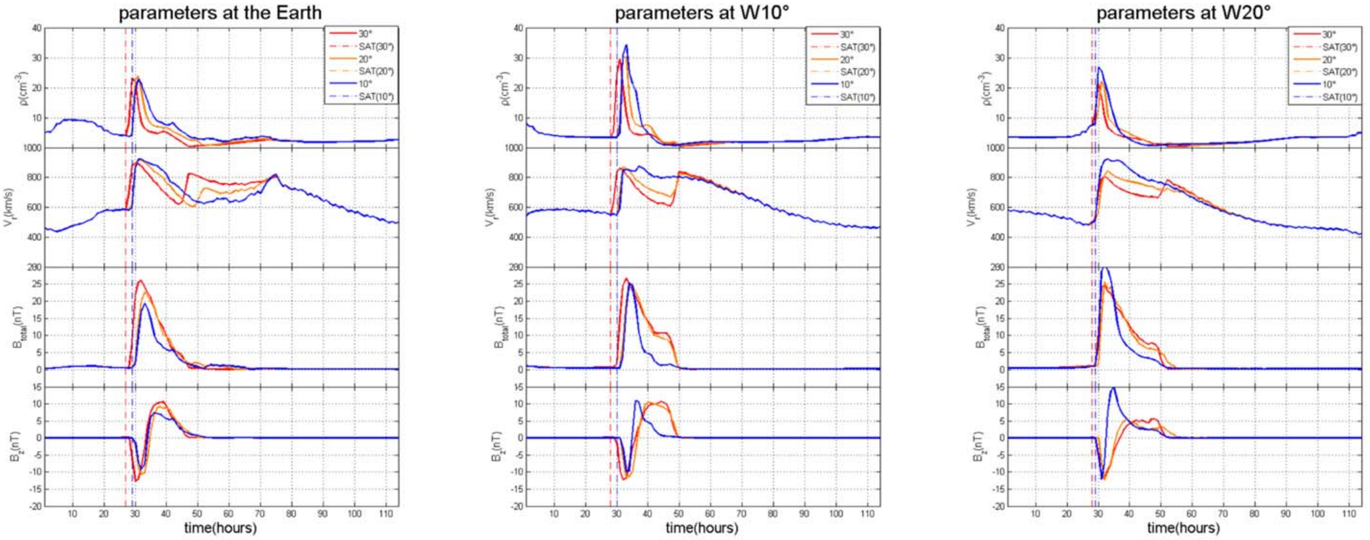

(a) Earth (b) $W10°$ (c) $W20°$

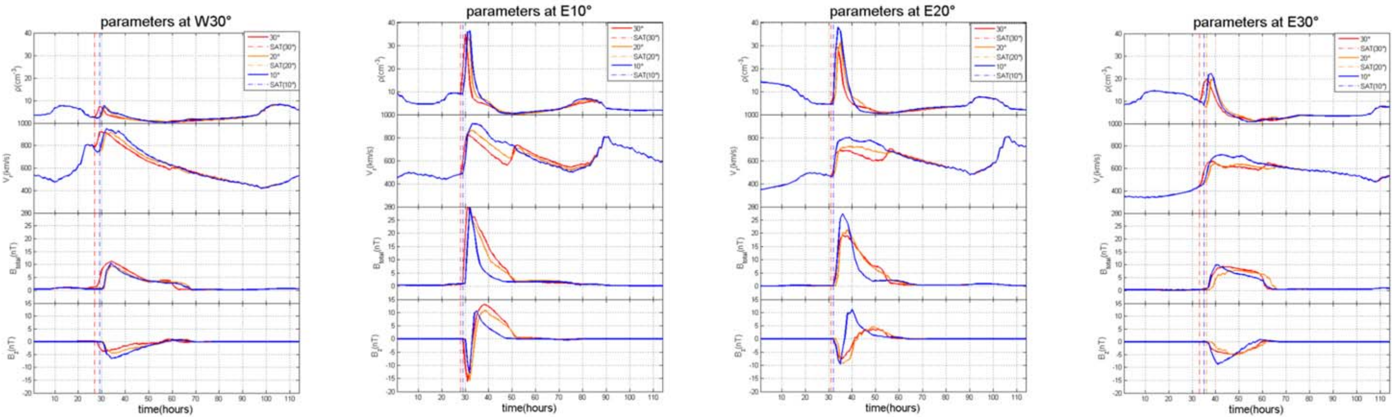

(d) $W30°$ (e) $E10°$ (f) $E20°$ (g) $E30°$

Figure 6. The profiles of plasma parameters—density, radial velocity, total magnetic field strength B_{total}, and B_z—at the Earth (a) and other locations with different longitudes (b)–(g) vs. time after CME launch. Solid lines with different colors refer to Cases 1–3 listed in Table 1 with different initial geometric dimensions: orange, blue, and red lines indicate Cases 1, 2, and 3, respectively. The shock arrival times of different CMEs are marked by dashed–dotted vertical lines with different corresponding colors.

Comparing panels (b) and (e), (c) and (f), and (d) and (g), in Figures 6 and 7, we notice that the peak values to the east are larger than those at the same longitudes to the west, which demonstrates the CME deflects to the east during its propagation for all five cases. From Figure 3(a), a distinct CIR structure can be found to the west of the CME; therefore, as the fast CME catches up with the CIR with relatively higher density and lower speed, it always deflects to the east (also see Liu et al. 2019).

4. Conclusions

In this study, we numerically investigated the influence of the initial parameters of CMEs on the simulation results at different latitudinal and longitudinal locations at 1 au. First, we established the steady-state interplanetary background solar wind for CR 2093 by using a 3D IN-TVD MHD model. Based on the GCS model, five groups of CMEs were chosen as test cases, and were injected into the background solar wind. The five cases included one standard case, two cases with varied geometry dimensions and density but the same mass as the standard case, and two cases with varied magnetic field strengths.

Then, we compared the simulation results of the five cases at 1 au at seven longitudinal locations, which are 0, *W*10, *W*20, *W*30, *E*10, *E*20, and *E*30; and seven latitudinal locations, which are 0, *N*10, *N*20, *N*30, *S*10, *S*20, and *S*30. As we discussed in Paper I, at the locations along the initial CME propagation, when the initial density and geometric dimensions of the CME are both changed, the propagation of the CME do not change significantly, as long as the total mass of the CME remains the same. However, at the locations away from the initial direction of the CME, the influence of the initial parameters on the simulation results is quite different. The main results of this study are summarized as follows:

(1) The change of the initial geometric dimension and magnetic field have different influences on the CME propagation process in the meridional and ecliptic planes. In the meridian plane of $\phi = 0°$, at 1 au, as the latitude of the observer changes within ±30°, the SATs of CMEs decrease significantly when the initial geometric thickness increases, or the initial

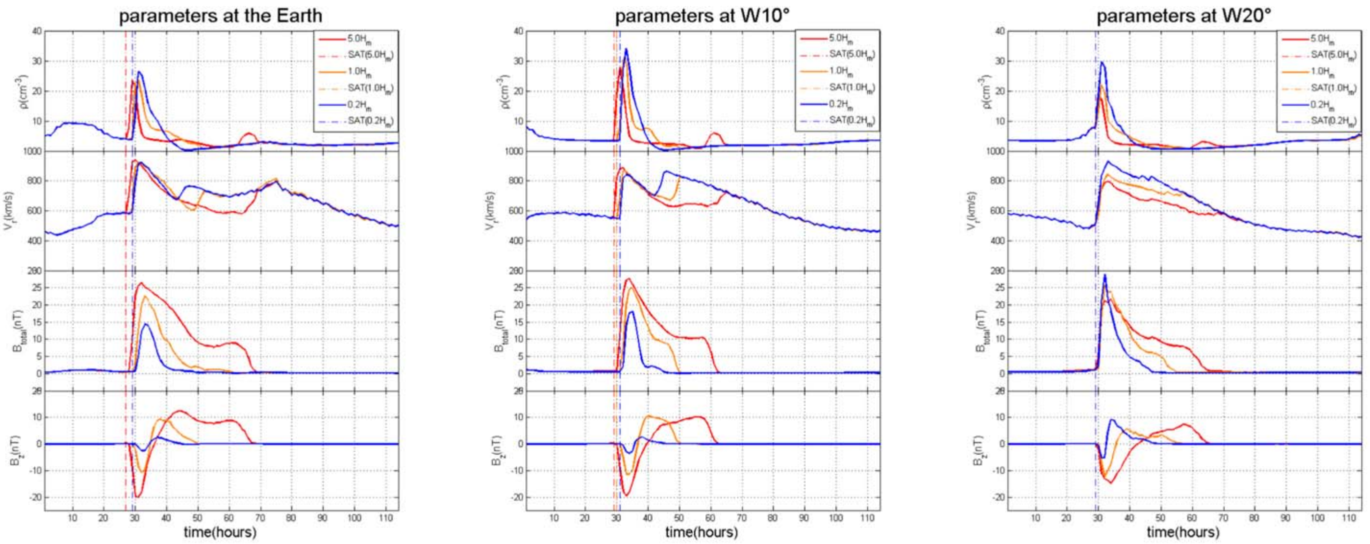

(a) Earth (b) $W10°$ (c) $W20°$

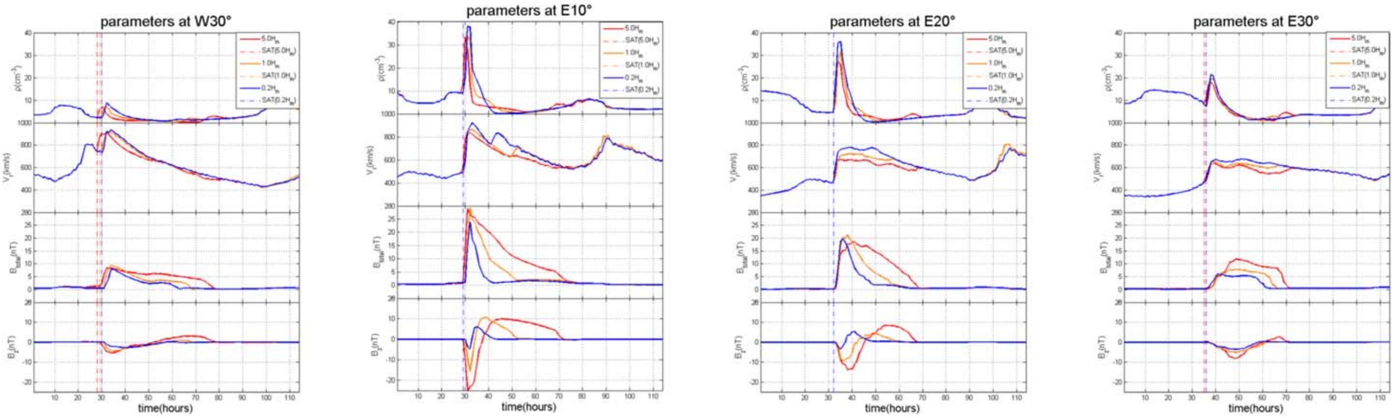

(d) $W30°$ (e) $E10°$ (f) $E20°$ (g) $E30°$

Figure 7. The profiles of plasma parameters—density, radial velocity, total magnetic field strength B_{total}, and B_z—at the Earth (a) and other locations with different longitudes (b)–(g) vs. time after CME launch. Solid lines with different colors refer to Cases 1, 4, and 5 listed in Table 1 with different initial magnetic field strength: orange, red, and blue lines indicate Cases 1, 4, and 5, respectively. The shock arrival times of different CMEs are marked by dashed–dotted vertical lines with different corresponding colors.

$B_{\max}$ increases. And the difference of SATs among Cases 1–3 increases with the enhancement of the latitude. At higher latitudes, the influence of the CME on the magnetic field is smaller than that on the fluid field.

(2) In the ecliptic plane, also at 1 au, as the longitude of the observer changed within ±30°, the SATs of CMEs almost remained unchanged as the initial geometric thickness increased, or the initial $B_{\max}$ increased. All the peak values at the CME shock decrease when the longitude increases. For all the plasma parameters, the difference of the cases with different geometric dimensions is small at all the locations with different longitudes. With the enhancement of the magnetic field strength, most of the peak values of density and radial velocity change slightly, but B_{total} and south of B_z of the CME increase obviously at different longitudinal locations.

(3) In general, as the initial CME mass remains unchanged, the initial δ affects the region of influence of the CME, and the difference in the latitudinal direction is more significant than that in the longitudinal direction.

(4) The simulation results also demonstrated that in all of the cases the CMEs were found to deflect to the south and the east when the CME propagates in the heliosphere. This deflection may due to the interaction between the fast CME and the CIR in front of it, as discussed by Liu et al. (2019). Studies of the CME deflection in the corona and heliosphere have been carried out by many authors, and the main factors leading to the CME deflection could be the influence of the ambient solar wind, such as the heliospheric current sheet, the streamers, the gradient of the corona magnetic energy density or the effect of the Lorentz force in the corona, the CIR structure and the difference between the CME speed and the solar wind speed in the heliosphere (e.g., Wang et al. 2004; Gui et al. 2011; Lugaz et al. 2011; Shen et al. 2011a; Wang et al. 2011; Zuccarello et al. 2012; Zhou & Feng 2013; Wang et al. 2014; Liu et al. 2019; Zhuang et al. 2019), or the interaction with other CMEs (e.g., Shen et al. 2011b; Lugaz et al. 2012).

As we know, the CME's initial parameters can affect the simulation results at different interplanetary locations during the CME propagation. In both Paper I and this work, we only consider the case in which the CMEs are launched along the Sun–Earth line and assume the initial CMEs have the GCS-model shape. As pointed out by Scolini et al. (2018), more complex CME shapes may have a larger impact on the in situ properties, and our GCS-based CME initial shapes are more similar to the actual CME shape than the spherical or spheroidal-like CME shapes. Because of the complexity of the initial CME shape, the choice of the geometric size is very important in modeling the propagation of CMEs. Our simulation results showed that when the initial mass of the CME models remained unchanged, the initial geometric thickness had different influence on the simulation results at 1 au at the locations with different latitudes and longitudes.

Besides the initial geometric parameters, density and magnetic field strength, there are still many controlling factors that should be considered. In the future, more extensive validation studies to test the influence of different solar wind background, different CME launched direction, and different CME speeds need to be applied for the GCS-based CME model.

The synoptic magnetogram data in this work were obtained from the Global Oscillation Network Group (GONG) of the National Solar Observatory. The numerical calculation has been completed on TianHe-1 (A) at the National Supercomputer Center in Tianjin, China. We acknowledge the use of them. This work is jointly supported by the Strategic Priority Research Program of the Chinese Academy of Sciences, Grant No. XDB 41000000, the National Natural Science Foundation of China (41774184, 41974202, and 42004146), and the Specialized Research Fund for State Key Laboratories.

ORCID iDs

Fang Shen https://orcid.org/0000-0002-4935-6679

References

Altschuler, M. D., & Newkirk, G. 1969, SoPh, 9, 131
Arge, C. N., Odstrcil, D., Pizzo, V., & Mayer, L, R. 2003, in Improved Method for Specifying Solar Wind Speed Near the Sun, Proc. Tenth Int. Solar Wind Conf. 679
Chané, E., Jacobs, C., van der Holst, B., Poedts, S., & Kimpe, D. 2005, A&A, 432, 331
Chané, E., van der Holst, B., Jacobs, C., Poedts, S., & Kimpe, D. 2006, A&A, 447, 727
Chen, P. F. 2011, LRSP, 8, 1
Cheng, X., Guo, Y., & Ding, M. 2017, ScChD, 60, 1383
Dasso, S., Mandrini, C., Demoulin, P., & Luoni, M. 2006, A&A, 455, 349
Feng, X., Yang, L., Xiang, C., Wu, S., & Zhou, Y. 2010, ApJ, 723, 300
Gui, B., Shen, C., Wang, Y., et al. 2011, SoPh, 271, 111
Hosteaux, S., Chané, E., & Poedts, S. 2019, A&A, 632, A89
Liu, Y., Shen, F., & Yang, Y. 2019, ApJ, 887, 150
Lugaz, N., Downs, C., Shibata, K., et al. 2011, ApJ, 738, 127
Lugaz, N., Farrugia, C., Davies, J., et al. 2012, ApJ, 759, 68
Lundquist, S. 1951, PhRv, 83, 307
Manchester, W. B., & van der Holst, B. 2014, PPCF, 56, 064006
Odstrcil, D., & Pizzo, V. 1999, JGR, 104, 28225
Schatten, K. H., Wilcox, J. M., & Ness, N. F. 1969, SoPh, 6, 442
Scolini, C., Verbeke, C., Poedts, S., et al. 2018, SpWea, 16, 754
Shen, C., Wang, Y., Gui, B., Ye, P., & Wang, S. 2011a, SoPh, 269, 389
Shen, F., Feng, X., Wang, Y., et al. 2011b, JGR, 116, A09103
Shen, F., Feng, X., Wu, S., Xiang, C., & Song, B. 2011c, JGR, 116, A04102
Shen, F., Feng, X., Wu, S. T., & Xiang, C. 2007, JGRA, 112, A04102
Shen, F., Liu, Y., & Yang, Y. 2021, ApJS, 253, 12
Shen, F., Shen, C., Wang, Y., Feng, X., & Xiang, C. 2013, GeoRL, 40, 1457
Shen, F., Shen, C., Zhang, J., et al. 2014, JGRA, 119, 7128
Shen, F., Yang, Z., Zhang, J., Wei, W., & Feng, X. 2018, ApJ, 866, 18
Shiota, D., & Kataoka, R. 2015, SpWea, 14, 56
Thernisien, A. 2011, ApJS, 194, 33
Thernisien, A., Howard, R., & Vourlidas, A. 2006, ApJ, 652, 763
Toriumi, S., & Wang, H. 2019, LRSP, 16, 3
Vandas, M., Odstrcil, D., & Watari, S. 2002, JGR, 107, A9
Wang, Y., Chen, C., Gui, B., et al. 2011, JGRA, 116, A9
Wang, Y., Shen, C., Wang, S., & Ye, P. 2004, SoPh, 222, 329
Wang, Y., Wang, B., Shen, C., Shen, F., & Lugaz, N. 2014, JGRA, 119, 5117
Webb, D. F., & Howard, T. A. 2012, LRSP, 9, 3
Zhou, Y., & Feng, X. 2013, JGRA, 118, 6007
Zhou, Y., & Feng, X. 2016, JGRA, 122, 1451
Zhuang, B., Wang, Y., Hu, Y., et al. 2019, ApJ, 876, 73
Zuccarello, F. P., Bemporad, A., Jacobs, C., et al. 2012, ApJ, 744, 66